# Supporting Information

**Yangyuan Zhang,†[a] Shilong Liu,†[a] Nannan Ji,[a] Lingzhi Wei,[a] Qiyang Liang,[a] Jiejie Li,[b]**

**Ziqi Tian,*[b] Jianwei Su*[a] and Qianwang Chen*[c]**

a Institutes of Physical Science and Information Technology, Key Laboratory of Structure and Functional Regulation of Hybrid Materials, Anhui University, Hefei 230601, China. E-mail: sujianwei@ahu.edu.cn
b Key Laboratory of Advanced Fuel Cells and Electrolyzers Technology of Zhejiang Province, Ningbo Institute of Materials Technology and Engineering, Chinese Academy of Sciences, Ningbo 315201, China. E-mail: tianziqi@nimte.ac.cn
c Hefei National Laboratory for Physical Science at Microscale, Department of Materials Science & Engineering, University of Science and Technology of China, Hefei 230026, China. E-mail: cqw@ustc.edu.cn
† These authors contributed equally to this work.

# Experimental Section

**Chemicals:** Cerium (III) nitrate hexahydrate ($Ce(NO_3)_3·6H_2O$, Aladdin Reagent Co., Ltd), bismuth nitrate pentahydrate ($Bi(NO_3)_3·5H_2O$, Aladdin Reagent Co., Ltd), Methanol anhydrous ($CH_3OH$, Sinopharm Chemical Reagent Co., Ltd), 1, 3, 5-benzenetricarboxylic acid ($H_3BTC$, Energy Chemical Co., Ltd), deuterated water ($D_2O$, Tenglong Weibo Technology Co., Ltd) and dimethyl sulfoxide (DMSO, Tenglong Weibo Technology Co., Ltd), Ar gas (99.999%), $CO_2$ gas (99.9995%), All the chemicals were used without further purification. The deionized water used in all experiments was with a specific resistance of 18.2 MΩ·cm.

**Preparation of Bi-BTC:** 1.2 g of $Bi(NO_3)_3·5H_2O$ and 1.6 g of $H_3BTC$ were added to 60 ml of a mixture of DMF and methanol (3:1 v/v), stirred for 30 min and then transferred to 100 ml of Teflon-lined stainless-steel autoclave, and then the reaction was carried out at 130 °C for 48 h. Finally, the suspension was centrifuged, washed three times with DMF, methanol, and deionized water, and then dried in an oven at 60 ℃ to obtain a white powder.

**Preparation of CeBi-BTC with different Ce contents:** 100 mg of Bi-BTC was dispersed in 40 ml of DMF, while 50, 100 and 150 mg of $Ce(NO_3)_3·6H_2O$ were dissolved in 20 ml of DMF, and then the latter was poured into the former and stirred for 24 h. Finally, $Ce_1$Bi-BTC, $Ce_2$Bi-BTC and $Ce_3$Bi-BTC were obtained by centrifugation and drying with different Ce contents, respectively.

**Preparation of Bi@C, $Ce_1$-Bi@C, $Ce_2$-Bi@C, and $Ce_3$-Bi@C:** The as-prepared Bi-BTC, $Ce_1$Bi-BTC, $Ce_2$Bi-BTC and $Ce_3$Bi-BTC four precursors was placed in the tube furnace and heated to 600 °C for 2 h in the Ar atmosphere. The heating rate was controlled at 5 °C $min^{-1}$. As-prepared black samples were directly used without any post-treatment.

**Characterization:** The powder X-ray diffraction patterns of the samples were analyzed with an X-ray powder diffraction (German Bruker D2 PHASE) using Cu-Kα radiation (λ = 1.54178 Å) with 2θ range of 10-80°. Morphologies and size of all as-synthesized samples were systematically characterized through scanning electron microscopy (SEM, Regulus 8230). Transmission electron microscopy (TEM) images were taken on a TEM (JEOL JEM-F200), equipped with Super-X energy dispersive X-ray (EDX) spectroscopy. X-ray photoelectron spectroscopy (XPS) analysis was carried out on an X-ray photoelectron spectrometer (ThermoFisher Escalab 250Xi) using Al-Kα radiation. Specific surface areas and pore diameters were determined from $N_2$ physisorption data at 77 K on an automated gas sorption analyzer (Quantachrome AutosorbiQ) by employing the Brunauer-Emmet-Teller (BET) and Barrett-Joyner-Halenda (BJH) methods, respectively. The content of Bi and Ce were obtained via the inductively coupled plasma-atomic emission spectrometry (ICP-AES) (ThermoFisher IRIS Intrepid II XSP)

**Electrocatalytic $CO_2$RR measurements:** The electrocatalytic $CO_2$RR measurements were carried out in a three-electrode system using an electrochemical work station (CHI 760E). Electrolysis were performed in a gastight two-compartment electrochemical H-type cell with Nafion-117 proton exchange membrane as a separator. The Ag/AgCl reference electrode (saturated KCl solution) was placed in the same chamber with the working electrode, while a platinum mesh counter electrode was placed in the other chamber. Each chamber consisted of 30 mL 0.1 M $KHCO_3$ solution with approximately 10 mL headspace. The working electrode was obtained by a typical preparation procedure that 80 μL homogeneous catalyst ink, in which 6.25 mg catalysts and 10 μL Nafion solution (5 wt. %) were dispersed into 490 μL deionized water and isopropanol mixed solution (2:1 v/v), was loaded onto a 1 cm ×1 cm carbon fiber paper with a 1 mg/$cm^2$ loading mass. Prior to $CO_2$RR reaction, the cathodic electrolyte was saturated with carbon dioxide at a flow rate of 20 mL/min for at least 30 min with a stirring rate of 500 rpm. Carbon dioxide was continuously bubbled into the cathodic electrolyte throughout the $CO_2$RR reaction and then vented directly into the gas sampling loop (1 mL) of a gas 3 chromatograph. LSV test was carried out with a scan rate of 5 mV/s. For the faradaic efficiency analysis, the gas products were detected by using an online gas chromatograph (Agilent 7890B) which could take gas samples every 30 min and the liquid product was detected by 1H NMR on an JNM-ECZ400S.

**Faradaic efficiency was calculated using the formula:**

$$FE = Q_{product}/Q_{total}$$

where $Q_{product}$ stands for the quantity of electric charge for $H_2$, CO or formate and $Q_{total}$ represents the total quantity of electric charge during the whole $CO_2$ reduction process. $Q_{product}$ and $Q_{total}$ were received from the following equations:

$$Q_{product} = Z_{product} \times F \times N_{product}\ Q_{total} = I \times t$$

where $Z_{product}$ stands for the number of transfer electrons, which was 2, 2 and 2 for $H_2$, CO and formate, respectively. F was the faraday constant (96485 C $mol^{-1}$). $N_{product}$ was determined by the moles of product, according to the standard curve line of GC and 1H NMR. I, received from the practical test current, represented the average electrocatalysis current during a fixed time (t) and t was a time for gas filling the GC sampling loop. The concentration of formate was obtained by using the calibration curve, which was plotted by using the peak area ratio (Formate/DMSO) versus the concentration standard solutions of formate.

**Density functional theory (DFT) calculations：**

Computational Methods and Details: We employed the Vienna Ab initio simulation package (VASP)[1-3] for conducting all spin-polarized density functional theory (DFT) calculations. The Perdew–Burke–Ernzerhof (PBE) generalized gradient approximation (GGA)[4, 5], a widely accepted functional known for its accurate prediction of the electronic structure of materials, was utilized to treat the exchange-correlation function. To mitigate interactions with their respective images, we introduced a 15 Å vacuum layer perpendicular to the interface. The plane-wave basis set energy cutoff was set to 500 eV, ensuring both accuracy and computational efficiency. For adequate sampling of the electronic band structure, Brillouin zone integrations were carried out using a 3 × 3 × 1 k-point mesh. To achieve electronic self-consistency, a criterion of $10^{-7}$ eV was employed, and a force convergence tolerance of 0.03 eV $Å^{-1}$ was utilized to ensure the accuracy and reliability of the calculated forces.

To further investigate the electronic charge transfer between atoms, we employed the atomic Bader charge analysis method, a reliable and widely-used technique for studying charge distribution in materials. The selection of these calculation parameters was meticulously considered to ensure the accuracy and reliability of our results. The comprehensive description of these computational methods guarantees the reproducibility and reliability of our research findings, based on the hydrogen electrode calculation model proposed by Nørskov et al.[6]

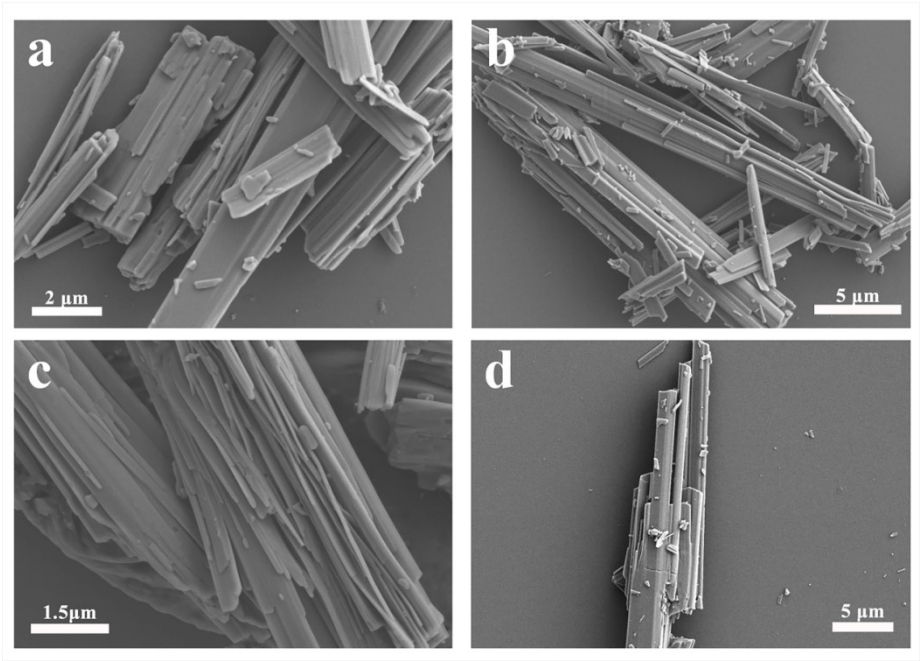


**Figure S1.** SEM images of (a) Bi-BTC, (b) $Ce_1$Bi-BTC, (c) $Ce_2$Bi-BTC and (d) $Ce_3$Bi-BTC.

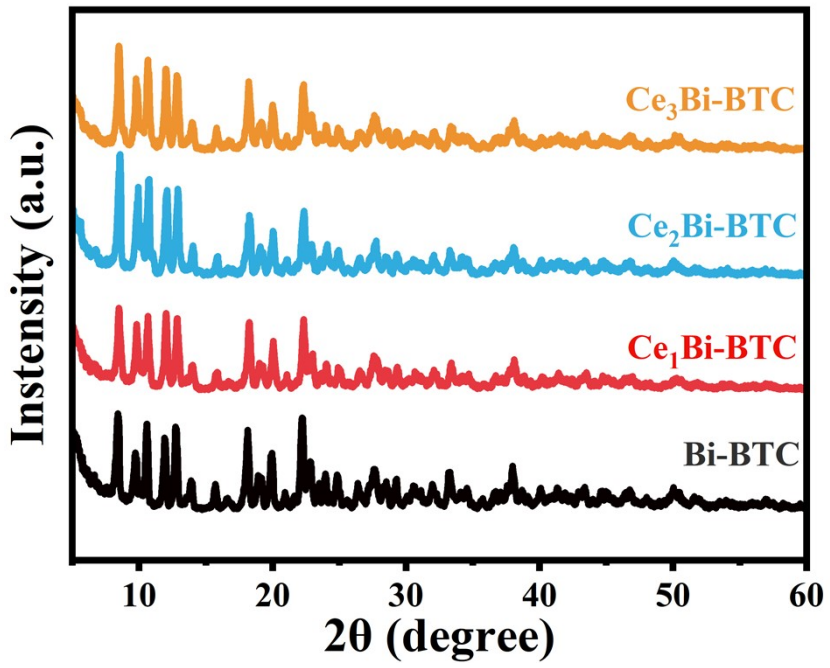


**Figure S2.** XRD patterns of (a) Bi-BTC, (b) $Ce_1$Bi-BTC, (c) $Ce_2$Bi-BTC and (d) $Ce_3$Bi-BTC.

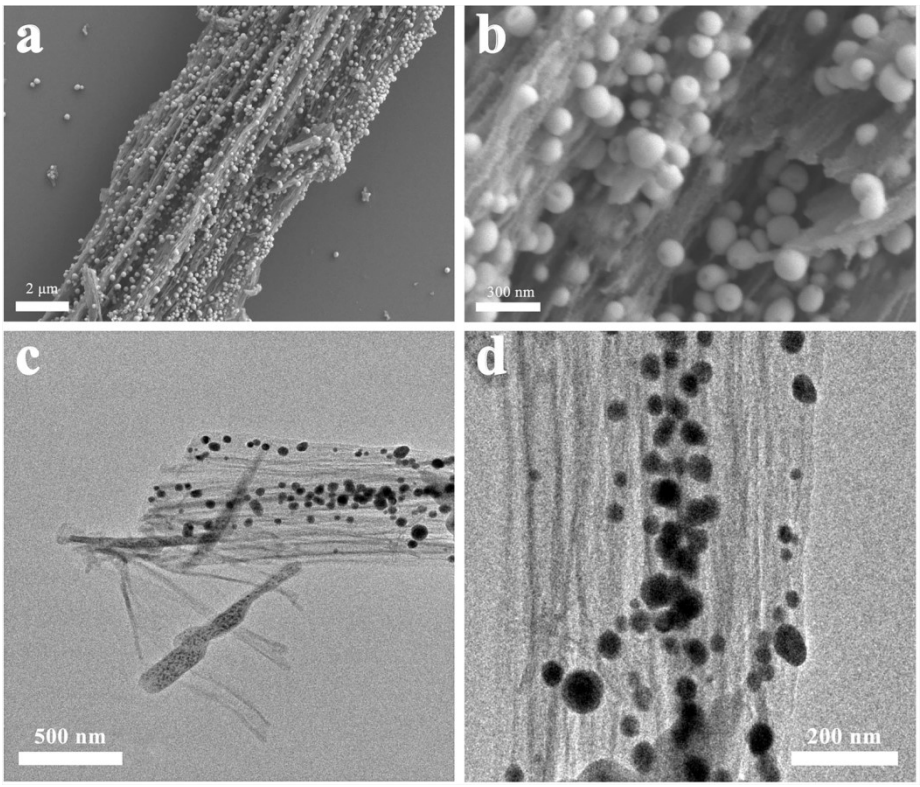


**Figure S3.** Morphology characterization of Bi@C. (a-b) SEM image. (c-d) TEM image.

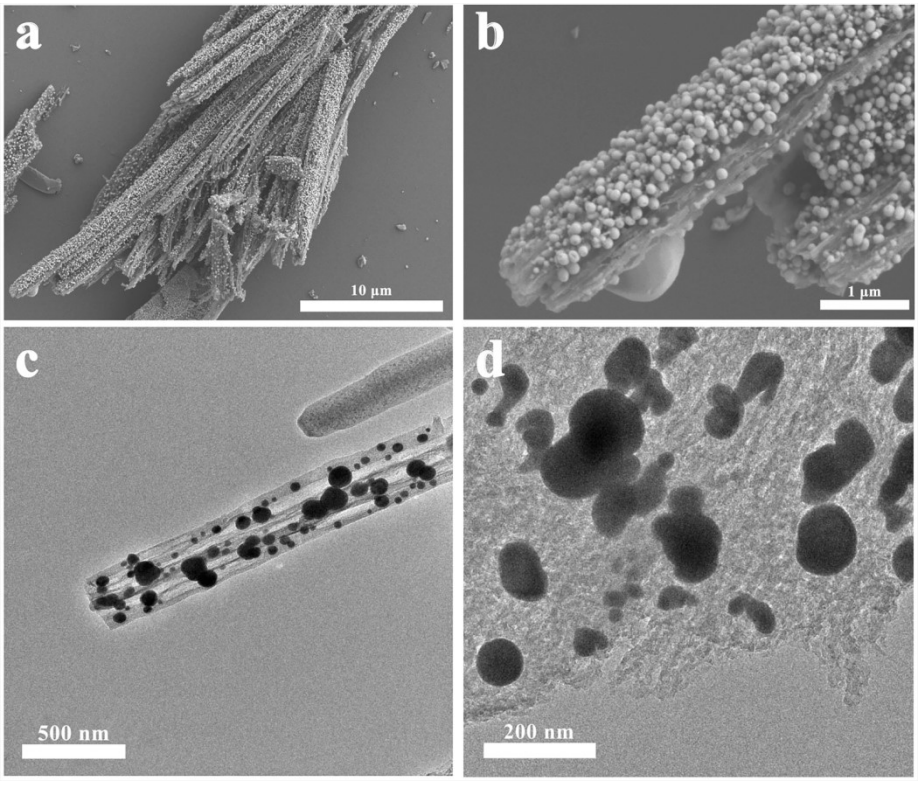


**Figure S4.** Morphology characterization of $Ce_1$-Bi@C. (a-b) SEM image. (c-d) TEM image.

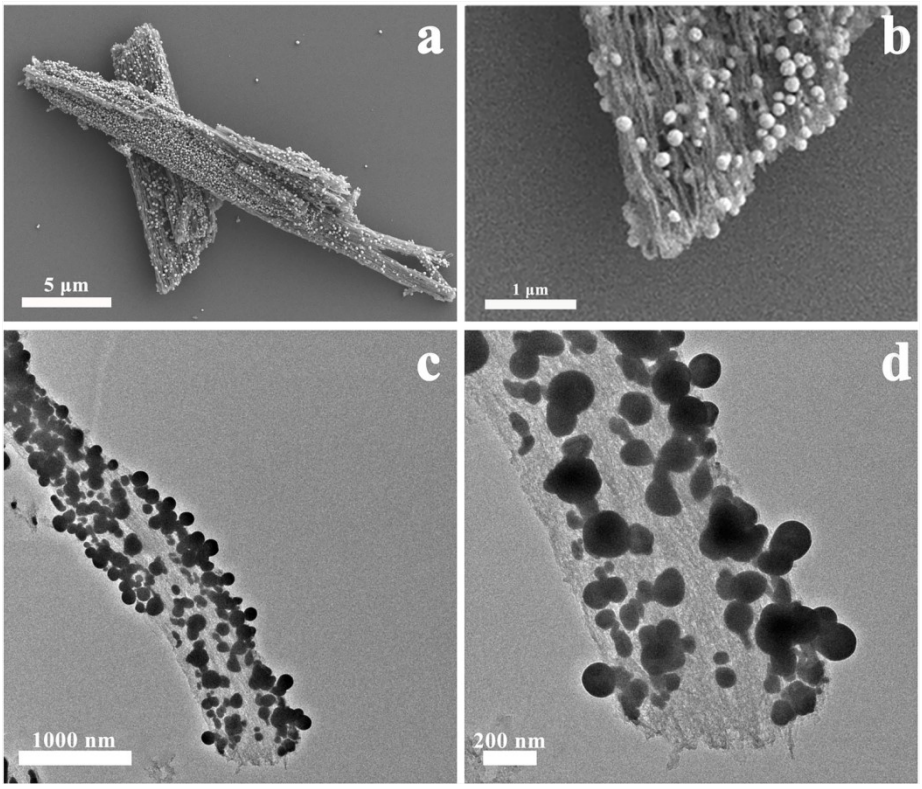


**Figure S5.** Morphology characterization of $Ce_3$-Bi@C. (a-b) SEM image. (c-d) TEM image.

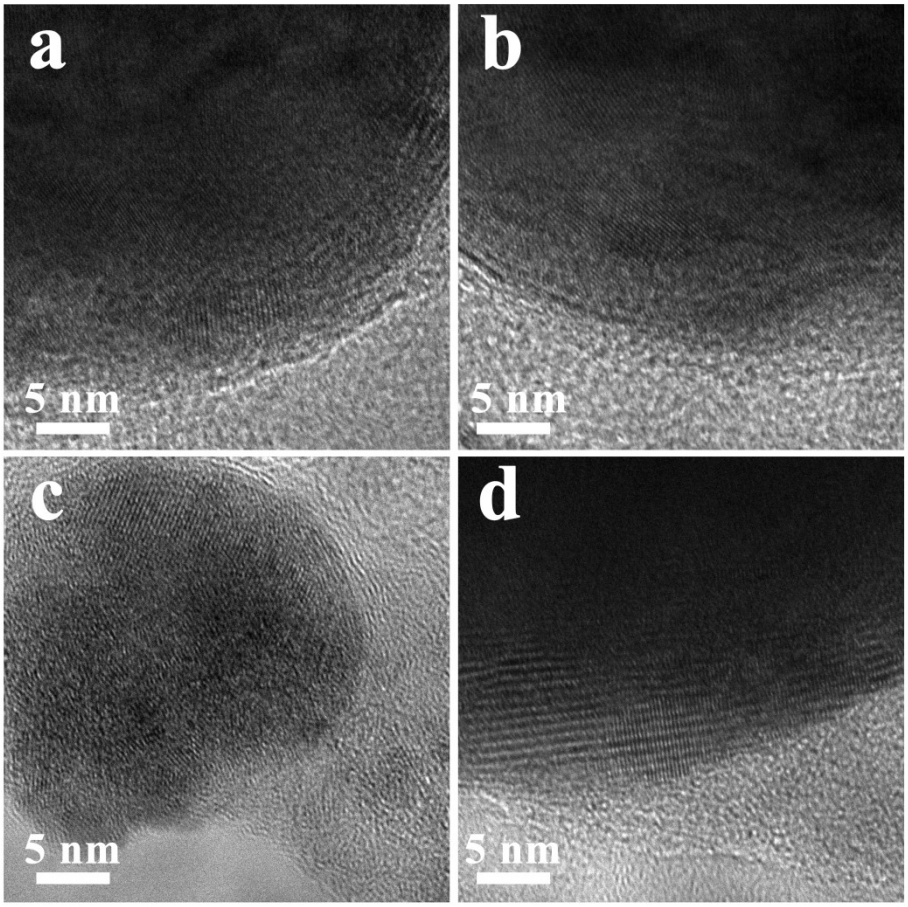


**Figure S6.** HRTEM images of $Ce_2$-Bi@C. It is evident that the Ce-Bi nanoparticles are not tightly enveloped by carbon layers, thereby facilitating rapid mass transfer throughout the porous carbon framework.

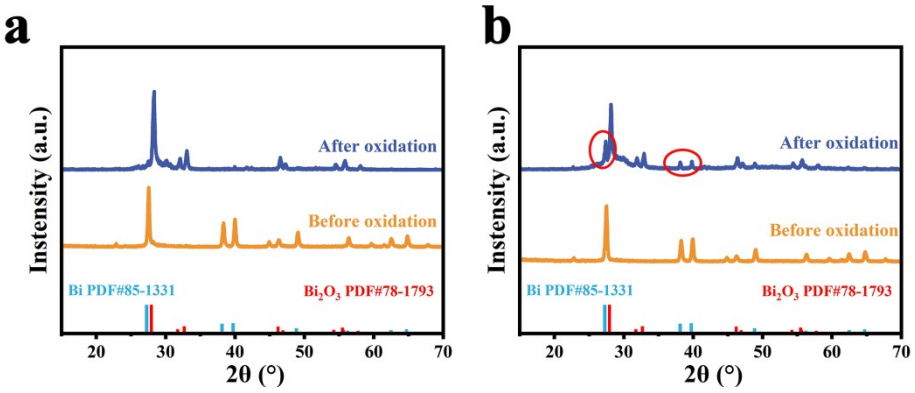


**Figure S7.** XRD patterns of (a) $Ce_2$-Bi@C and (b) Bi@C before and after oxidation at 200°C for 30 minutes in air atmosphere.

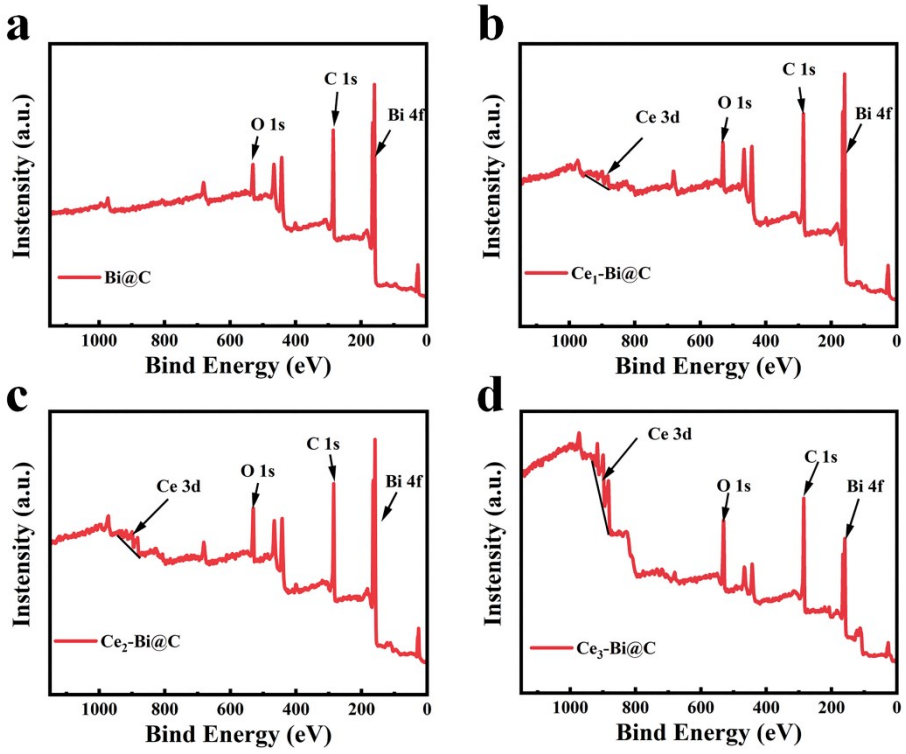


**Figure S8.** The XPS spectra of (a) Bi@C, (b) $Ce_1$Bi@C, (c) $Ce_2$Bi@C and (d) $Ce_3$Bi@C.

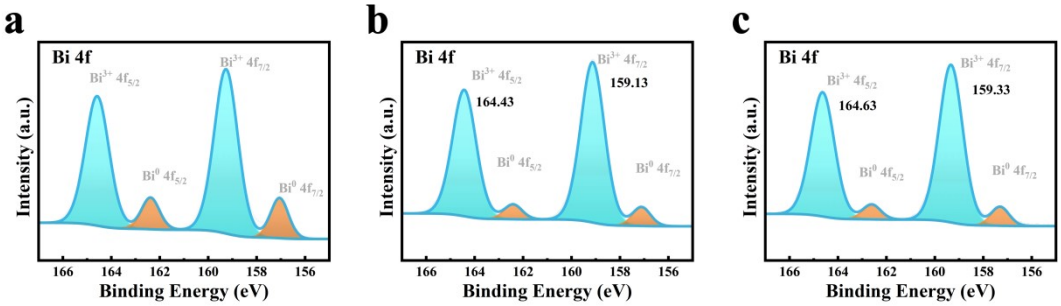


**Figure S9.** XPS spectra for the Bi 4f region of (a) Bi@C, (b) $Ce_1Bi@C$ and (b) $Ce_3Bi@C$.

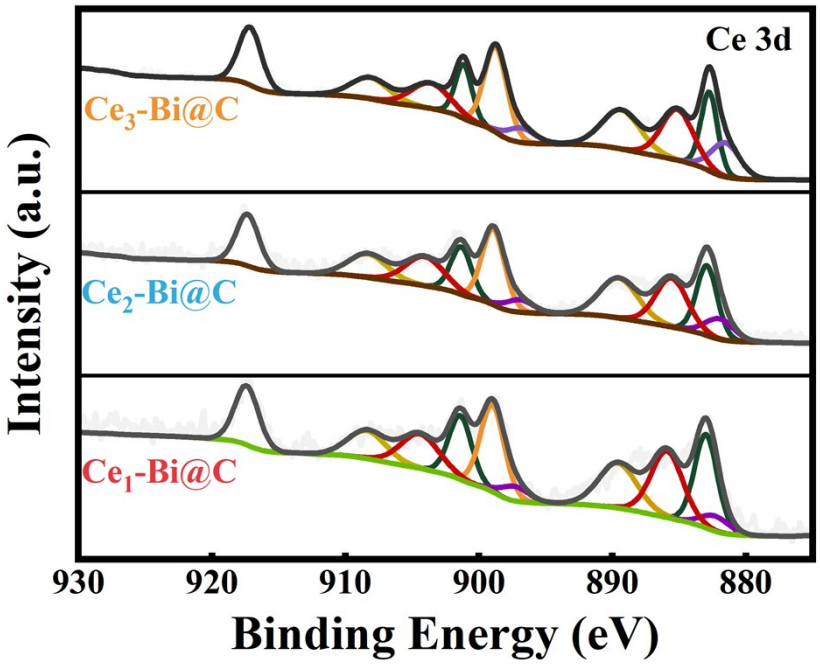


**Figure S10.** XPS spectra for the Ce 3d region.

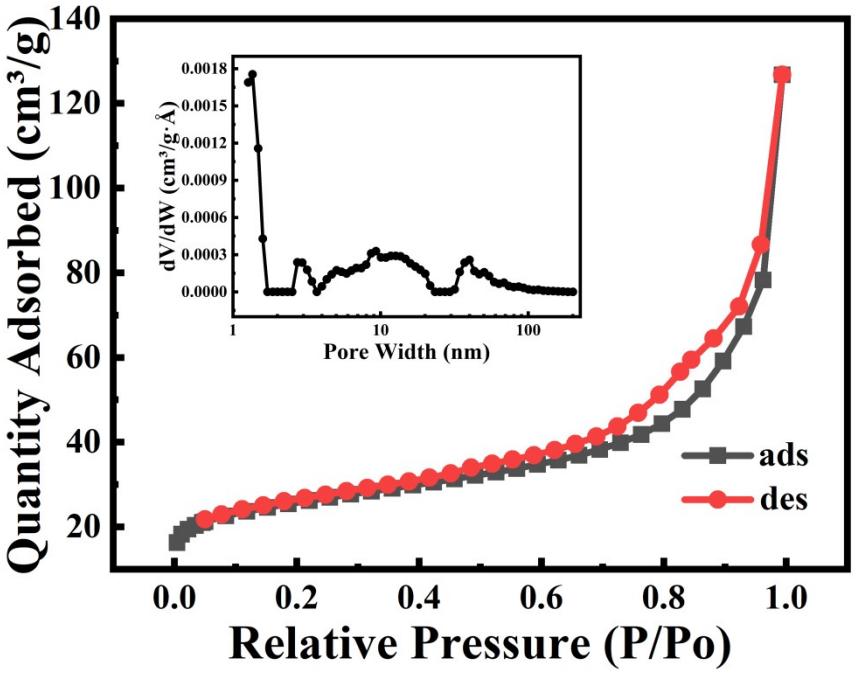


**Figure S11.** $N_2$ adsorption-desorption isotherms (inset: pore size distribution) of the $Ce_2$-Bi@C. the Brunauer-Emmett-Teller (BET) analysis was conducted on $Ce_2$-Bi@C, uncovering the abundant existence of multiple mesopores structures within the carbon layer, with the pore sizes mainly distributed in three ranges of ~3 nm, 4-20 nm and 25-50 nm. Moreover, the isotherm exhibits a type IV curve with a special surface area of 86.3 $m^2$ $g^{-1}$, indicating the presence of mesopores, which is beneficial for facilitating mass transfer and exposing more Bi active sites.

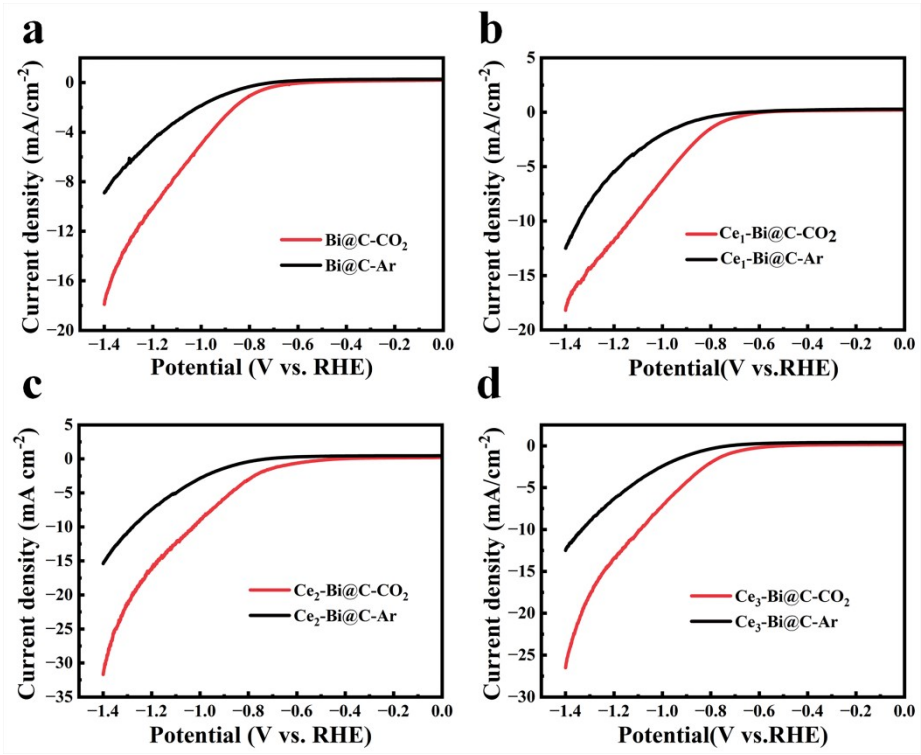


**Figure S12.** LSV curves of (a) Bi@C, (b) $Ce_1$Bi@C, (c) $Ce_2$Bi@C and (d) $Ce_3$Bi@C in the Ar or $CO_2$-saturated 0.1 M $KHCO_3$ electrolyte at a scan rate of 10 mV $s^{-1}$.

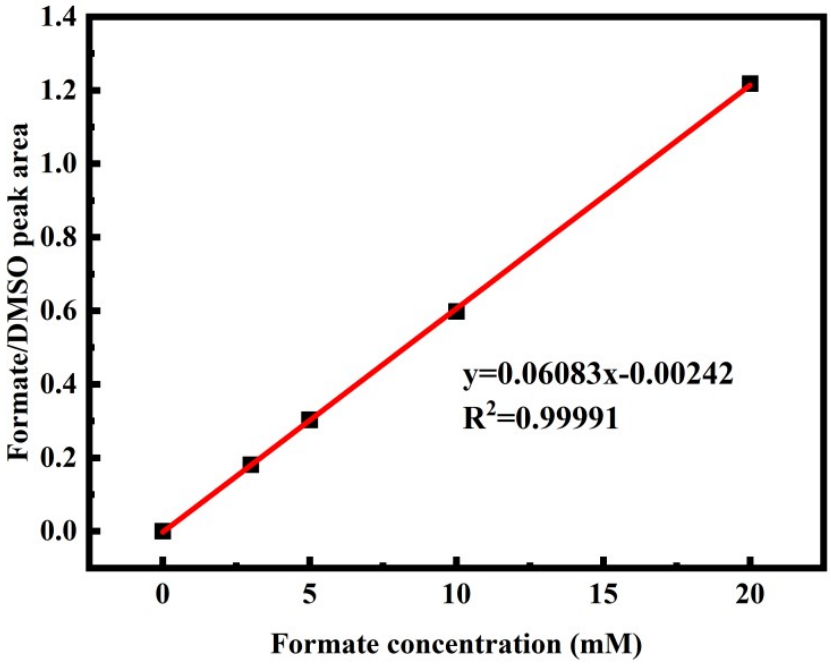


**Figure S13.** the standard curve of formic ($HCOO^-$). The ratio of formate peak area to DMSO peak area are compared to standard curve to quantify the concentrations of the formate products. The standard solution is prepared by mixing 0.1 mL of $D_2O$ with 0.5 mL of $KHCO_3$ solution containing formic acid and 0.002 mL of $KHCO_3$ solution containing DMSO (2.5% vol.).

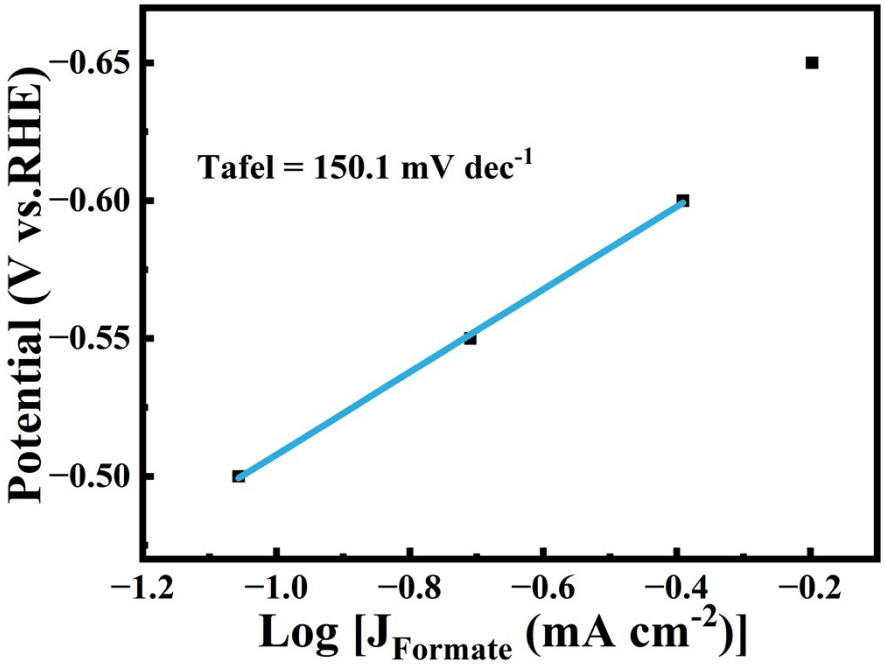


**Figure S14.** Tafel plots for producing $HCOO^-$ over the $Ce_2$-Bi@C in $CO_2$-saturated 0.1 M $KHCO_3$ electrolyte. A slope of 118 mV $dec^{-1}$ signifies that an initial single-electron transfer process ($CO_2 + e^- \rightarrow CO_2^{\bullet-}$) is the rate-determining step. Herein, the $CO_2$-to-formate Tafel slope of $Ce_2$-Bi@C was 150.1 mV $dec^{-1}$. Although it is higher than 118 mV $dec^{-1}$, it is likely to imply that an initial electron transfer rate might be the determining step during $CO_2$RR.

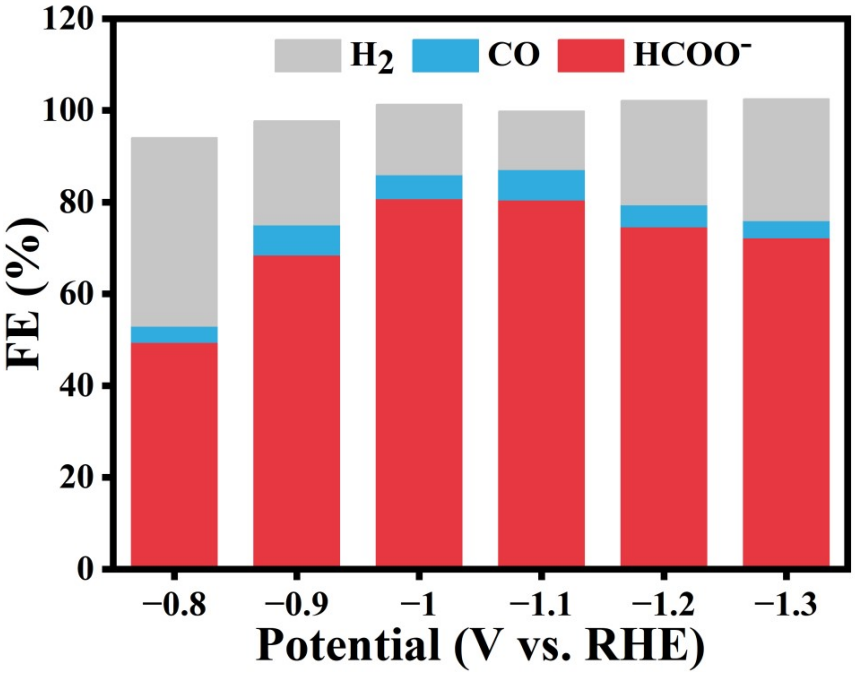


**Figure S15.** Faradaic efficiencies of the reduction products generated by Bi@C in 0.1 M $CO_2$-saturated $KHCO_3$ aqueous solution at different applied potentials.

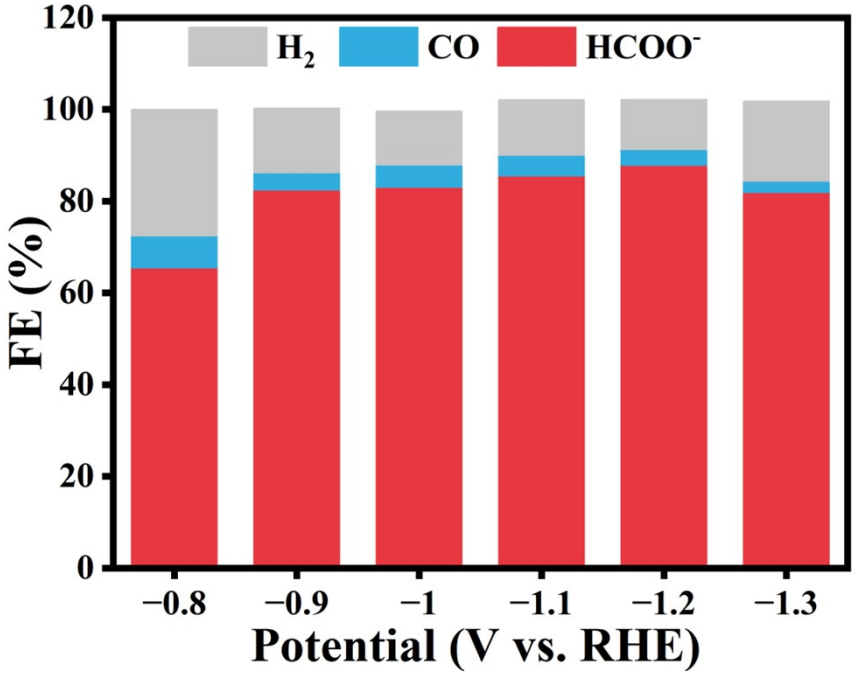


**Figure S16.** Faradaic efficiencies of the reduction products generated by $Ce_1$-Bi@C in 0.1 M $CO_2$-saturated $KHCO_3$ aqueous solution at different applied potentials.

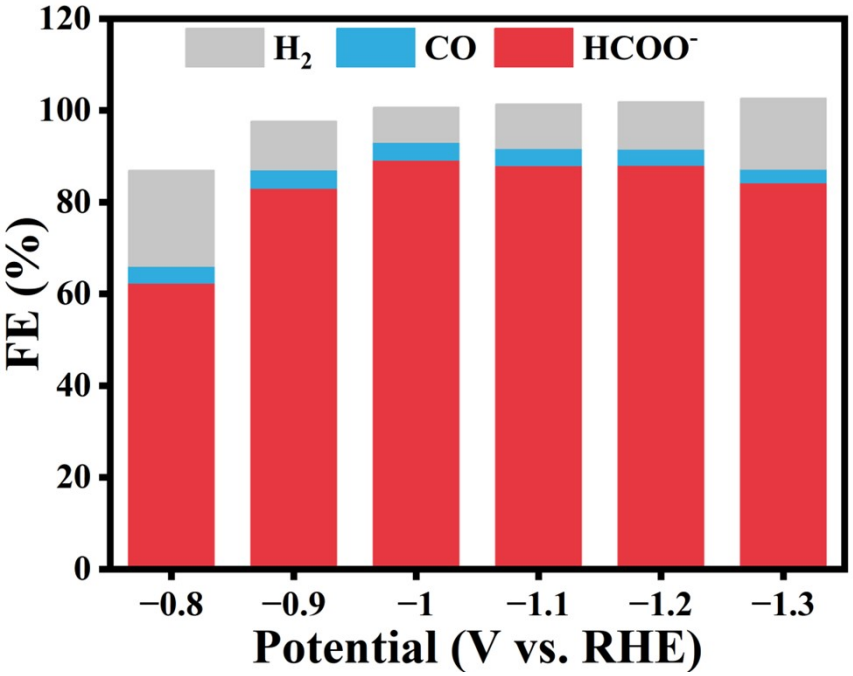


**Figure S17.** Faradaic efficiencies of the reduction products generated by $Ce_3$-Bi@C in 0.1 M $CO_2$-saturated $KHCO_3$ aqueous solution at different applied potentials.

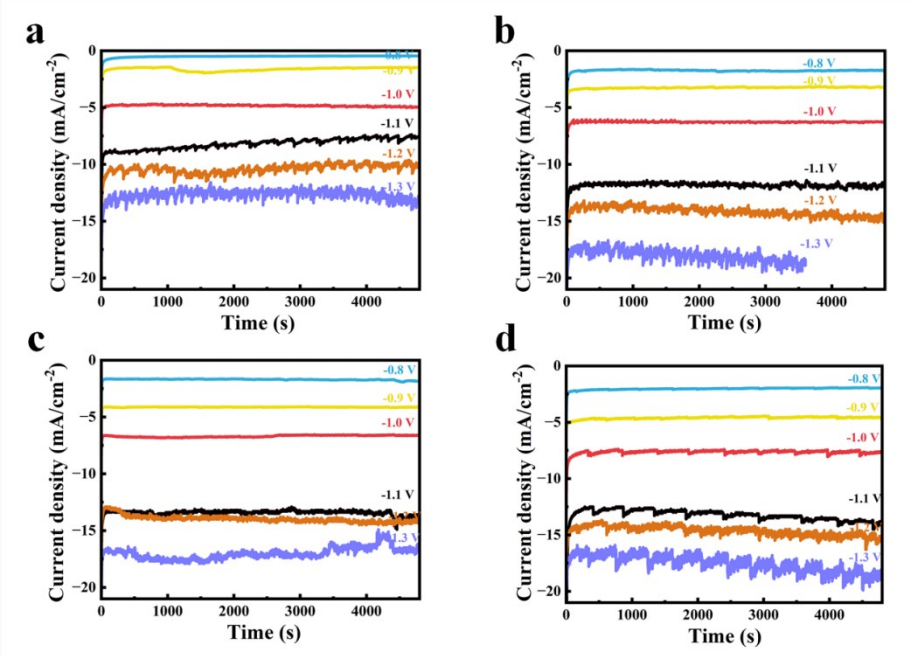


**Figure S18.** Chronoamperometry curves at various potentials in $CO_2$-saturated 0.1 M $KHCO_3$ over (a) Bi@C, (b) $Ce_1$-Bi@C, (c) $Ce_2$-Bi@C and (d) $Ce_3$-Bi@C.

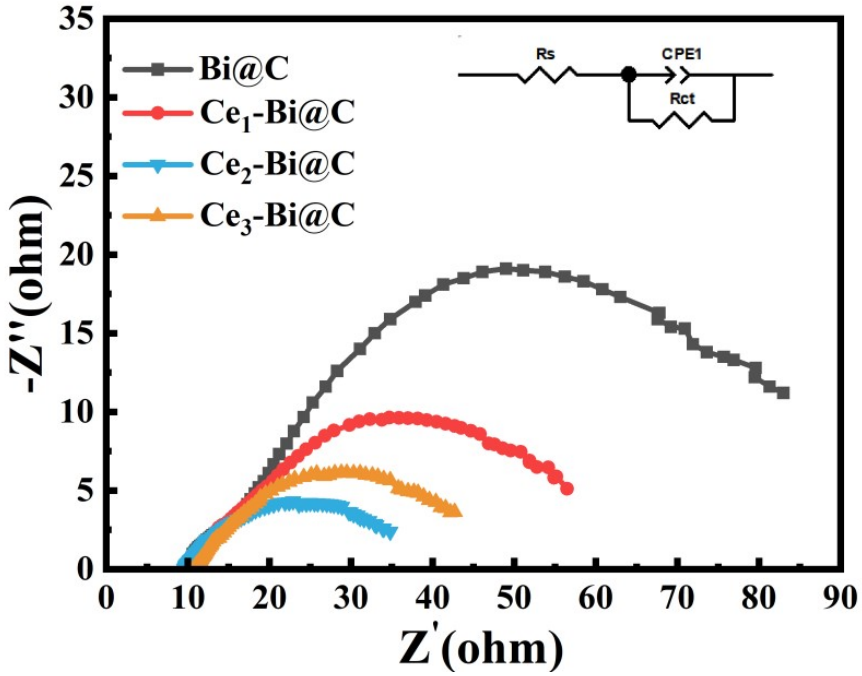


**Figure S19.** Electrochemical impedance spectroscopy (EIS) Nyquist plots for Bi@C, $Ce_1$-Bi@C, $Ce_2$-Bi@C and $Ce_3$-Bi@C collected in frequency range of 0.01-$10^6$ Hz.

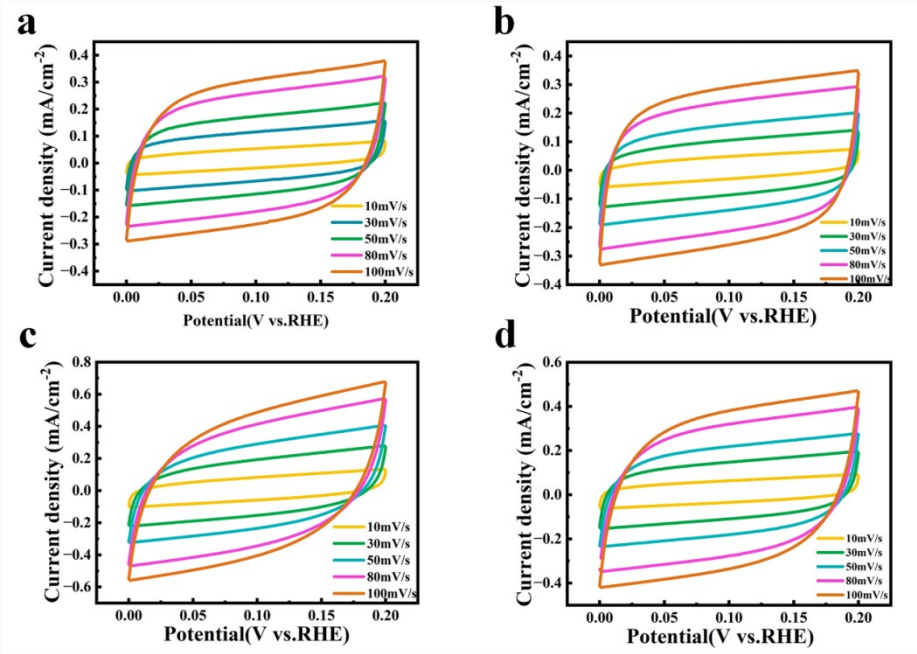


**Figure S20.** CV curves at range from 0 to 0.20 V with different scan rates (10, 30, 50, 80 and 100 mV·$s^{-1}$) for (a) Bi@C, (b) $Ce_1$-Bi@C, (c) $Ce_2$-Bi@C and (d) $Ce_3$-Bi@C, respectively.

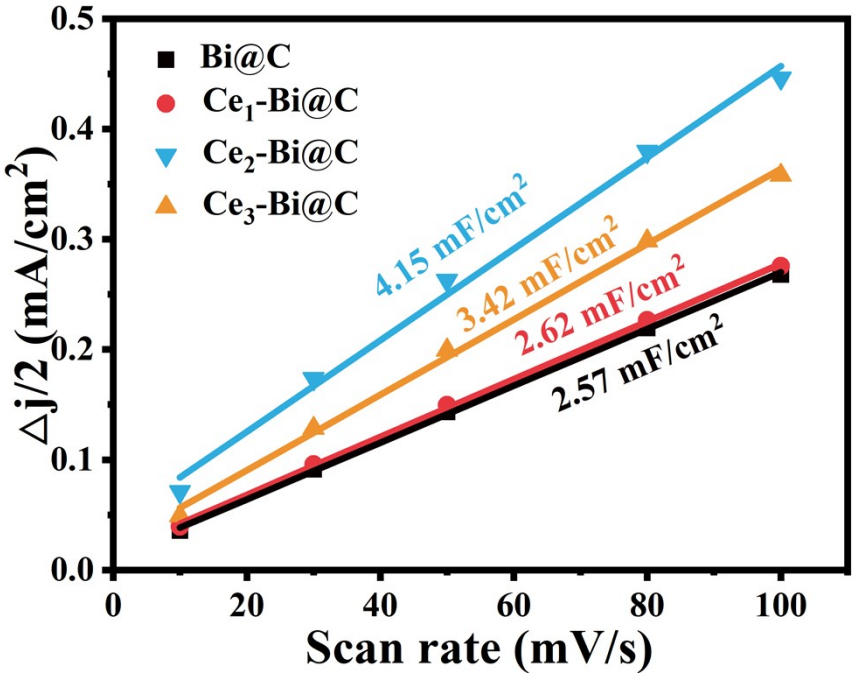


**Figure S21.** The electrochemical double layer capacitance per square centimeter of electrode derived from the CV curves. The slope of the curve in the figure represents the double-layer capacitance value ($C_{dl}$), and the larger the $C_{dl}$, the greater the electrochemical active area (ECSA).

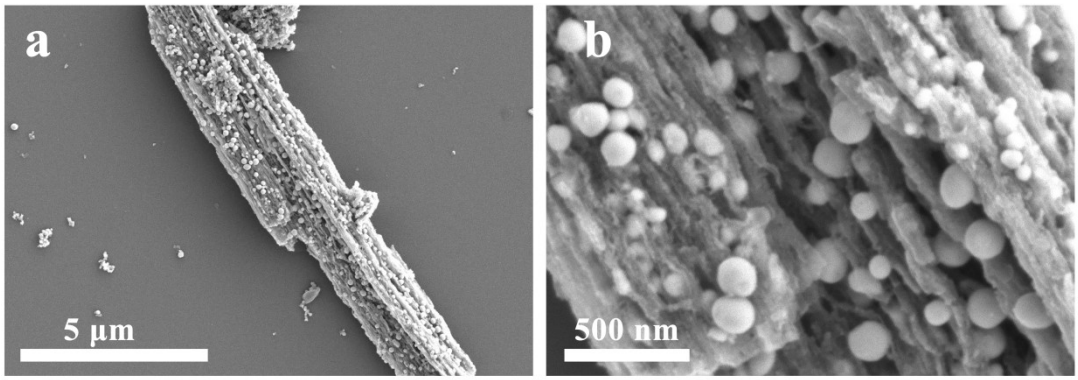


**Figure S22.** SEM images of $Ce_2$-Bi@C after 48 h stability test at -1.1 V vs. RHE.

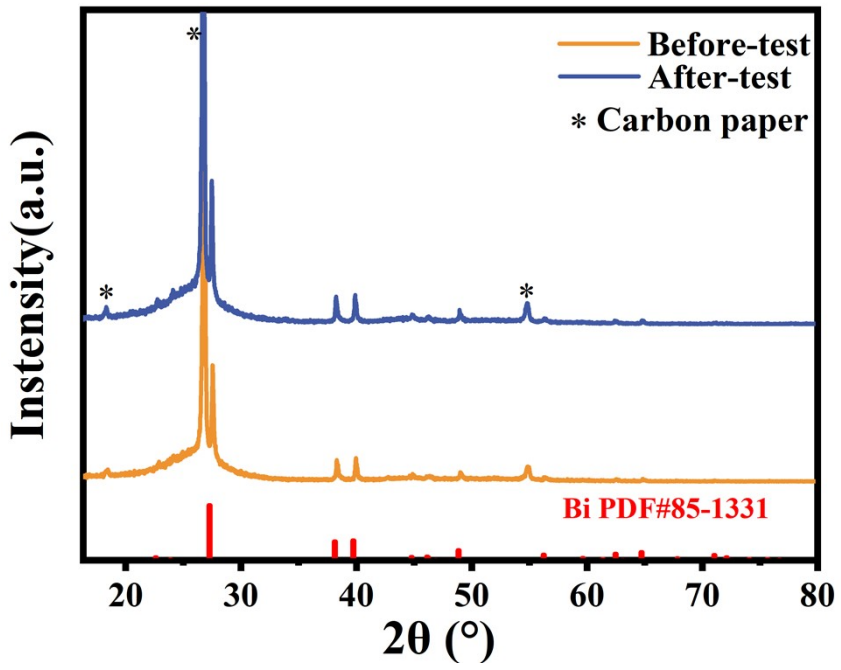


**Figure S23.** XRD patterns of $Ce_2Bi$@C before and after 48 h $CO_2$RR test at -1.1 V vs. RHE.

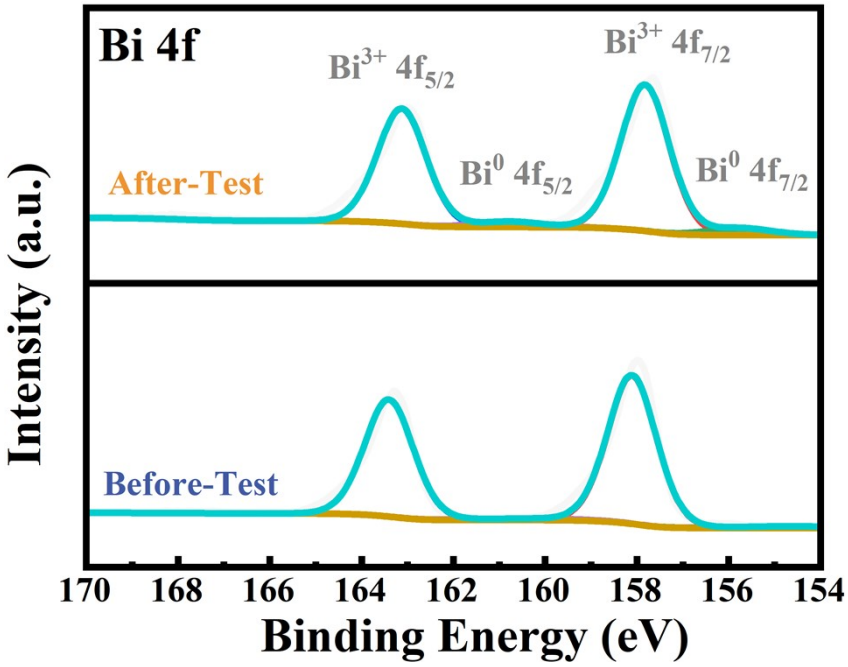


**Figure S24.** XPS patterns of $Ce_2Bi$@C before and after 48 h $CO_2$RR test at -1.1 V vs. RHE. The test results of this patterns were obtained by testing samples loaded with carbon paper.

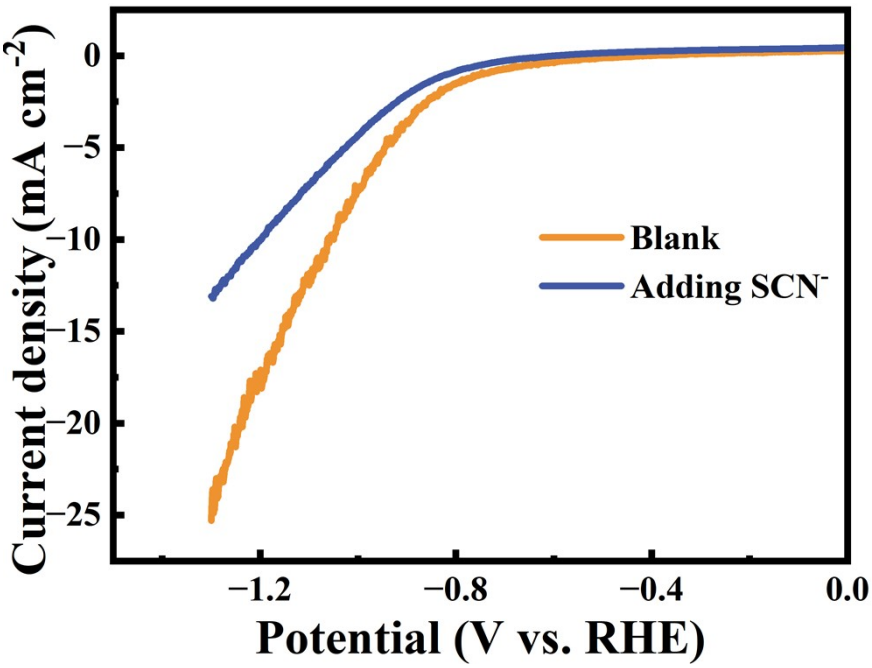


**Figure S25:** LSV curves before and after $SCN^-$ toxicity test. To demonstrate that $CO_2RR$ occurs on the Ce-Bi surface, we conducted a metal poisoning experiment. In our $CO_2RR$ testing, we added 1 mL of 0.5 M NaSCN solution to the $CO_2$-saturated $KHCO_3$ solution during the LSV test.[7] The results demonstrate a marked reduction in current subsequent to the introduction of $SCN^-$. This finding not only validates the role of Ce-Bi as the active site rather than the carbon substrate but also suggests that the carbon layer does not hinder ion diffusion, allowing for easy contact between $SCN^-$ with inner Ce-Bi nanoparticles.

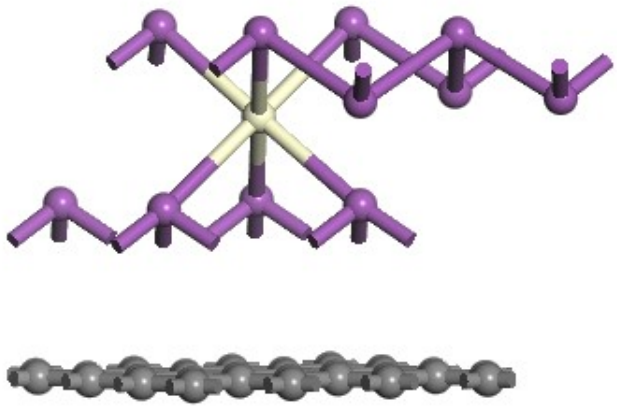

**Figure S26.** The heterogeneous doubled-layer model. To take into account the influence of the carbon matrix, we constructed a heterogeneous double-layered model. On the carbon layer side, the formation of *OCHO and *COOH are both highly endothermic, with free energy changes of 1.95eV and 2.0 eV, respectively. On the other hand, the formation energy of *OCHO on the metal layer side doesn't change much (0.71 eV with carbon *vs.* 0.72 eV w/o carbon). Thus even considering the carbon matrix, the simulation results still suggest that the $CO_2RR$ process takes place on the Ce-doped Bi nanoparticles, rather than the carbon matrix. The carbon matrix does not significantly affect the $CO_2RR$ process, but primarily serves as a support and encapsulating material to enhance the stability and dispersibility of the nanoparticles, as demonstrated in the experimental discussion.

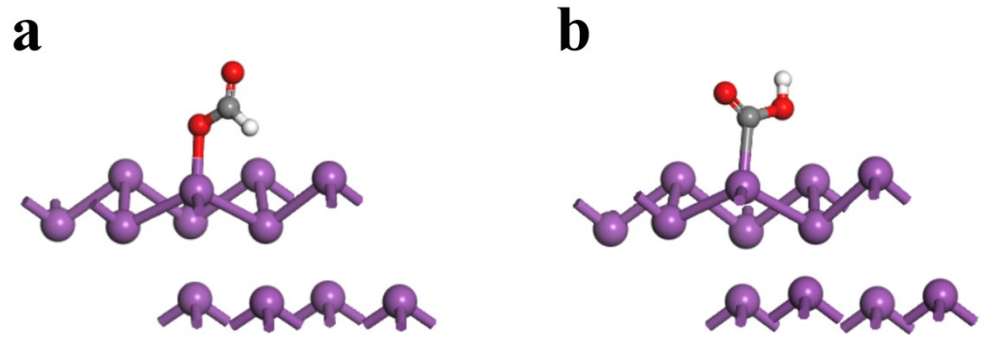


**Figure S27.** The adsorption configurations of (a) *OCHO (Bi) and (b) *COOH (Bi) species. (Purple, grey, red, and white colors represent Bi, C, O, and H atoms, respectively).

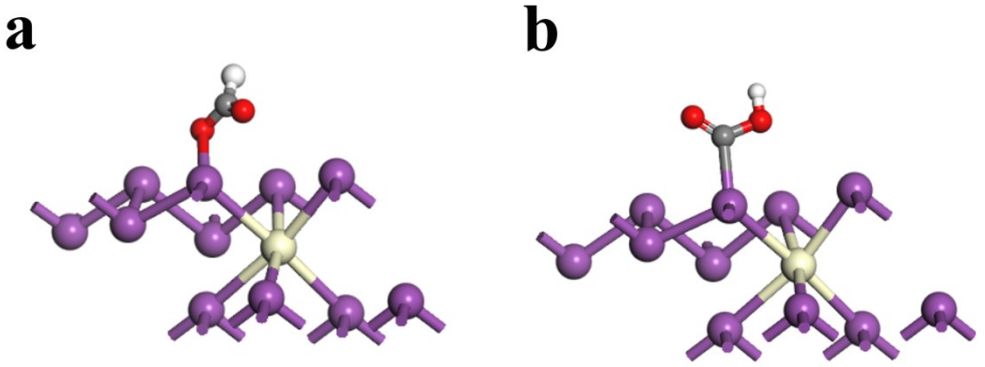


**Figure S28.** The adsorption configurations of (a) *OCHO (Ce-Bi) and (b) *COOH (Ce-Bi) species. (Purple, grey, red, and white colors represent Bi, C, O, and H atoms, respectively).

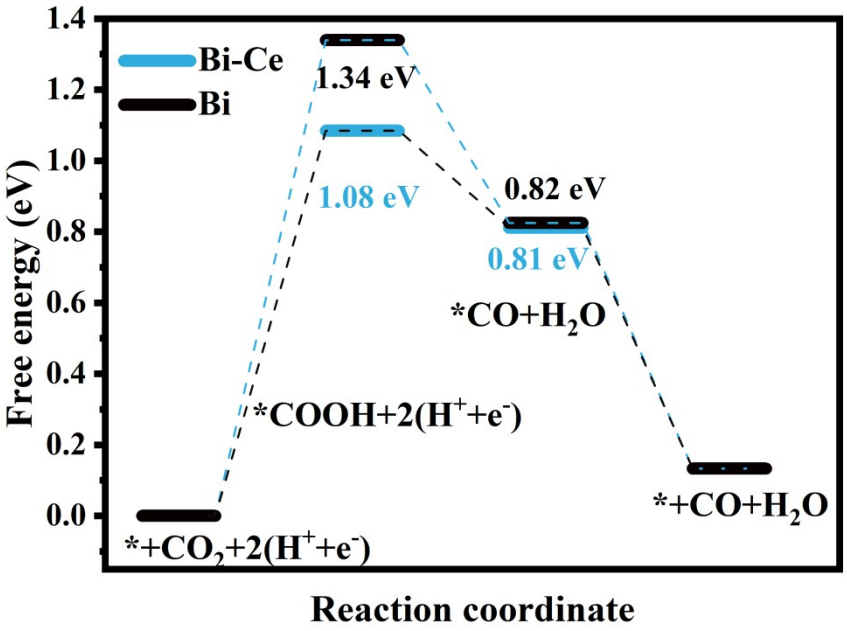


**Figure S29.** Gibbs free energy diagrams for CO on the surface of Ce-Bi and Bi.

**Table S1.** The ICP analysis of Bi, Ce in Bi@C, $Ce_1$-Bi@C, $Ce_2$-Bi@C and $Ce_3$-Bi@C

| samples | Ce | Bi |
|---|---|---|
| **Bi@C** | **-------** | **88.7 wt.%** |
| **$Ce_1$-Bi@C** | **1.15 wt.%** | **90.5 wt.%** |
| **$Ce_2$-Bi@C** | **4.09 wt.%** | **87.3 wt.%** |
| **$Ce_3$-Bi@C** | **6.02 wt.%** | **80.3 wt.%** |

**Notes and references**


1. P. E. Blöchl, *Phys. Rev. B*, 1994, **50**, 17953.
2. G. Kresse and J. Furthmüller, *Phys. Rev. B*, 1996, **54**, 11169.
3. G. Kresse and D. Joubert, *Phys. Rev. B*, 1999, **59**, 1758.
4. J. P. Perdew, K. Burke and Y. Wang, *Phys. Rev. B*, 1996, **54**, 16533.
5. J. P. Perdew, K. Burke and M. Ernzerhof, *Physical review letters*, 1996, **77**, 3865.
6. A. A. Peterson, F. Abild-Pedersen, F. Studt, J. Rossmeisl and J. K. Nørskov, *Energy Environ. Sci.*, 2010, **3**, 1311-1315.
7. Q. Wang, Z. Y. Zhou, Y. J. Lai, Y. You, J. G. Liu, X. L. Wu, E. Terefe, C. Chen, L. Song, M. Rauf, N. Tian and S. G. Sun, *J. Am. Chem. Soc.*, 2014, **136**, 10882-10885.